Supporting Information

Nanomechanical Encoding Method Using Enhanced Thermal Concentration on a Metallic Nanobridge

Jeong Oen Lee[1]†, Kwang-Wook Choi[1], Seon-Jin Choi[2], Min-Ho Kang[3], Min-Ho Seo[1], Il-Doo Kim[2], Kyoungsik Yu[1], and Jun-Bo Yoon[1]*

[1] School of Electrical Engineering, Korea Advanced Institute of Science and Technology (KAIST), 291 Daehak-ro, Yuseong-gu, Daejeon 34141, Republic of Korea

[2] Department of Materials Science and Engineering, Korea Advanced Institute of Science and Technology (KAIST), 291 Daehak-ro, Yuseong-gu, Daejeon 34141, Republic of Korea

[3] National NanoFab Center (NNFC), 291 Daehak-ro, Yuseong-gu, Daejeon, 34141, Republic of Korea

*Correspondence to: jbyoon@kaist.ac.kr

† Present address: Department of Electrical Engineering, California Institute of Technology, Pasadena, CA 91125, USA.

1. Fabrication Process

The fabrication began with an 8-inch silicon wafer on which a thermal oxide layer (10-nm-thick SiO_2) was deposited as a stress-buffering layer. Then, a silicon nitride (SiN) layer of 50 nm in thickness was deposited. A tungsten layer of 20 nm in thickness was deposited and then patterned to form the bottom electrodes. Because of its high etching selectivity, SiO_2 was employed as a sacrificial layer, which was deposited via a high-density-plasma chemical vapor deposition (HDP-CVD) method. Typically, the sacrificial layer has a step profile that follows the surface profile of the bottom electrode's patterns. To permit the accurate evaluation of the device's characteristics, we performed a surface-planarization process to remove this step profile on the suspended electrode. For example, if the target thickness of the sacrificial layer was 50 – 70 nm, we deposited a sacrificial layer of twice this thickness and then performed chemical-mechanical polishing (CMP). After the planarization process, the suspended electrode was formed by sputtering a 40-nm-thick layer of tungsten on top of the sacrificial layer. Figure S1a shows a cross-sectional TEM image of the fabricated device. Finally, the sacrificial SiO_2 layer was removed by dipping in a buffered oxide etchant (BOE) solution for 1 min. The residual stress in the sputtered tungsten layer provided the initial downward deflection after the release process. In Figure S1b, the bent shape of the nanomechanical beam is shown in a side-view image. During the release process, if the suspended structure is robustly designed, the sample can be released using a hot isopropyl alcohol (IPA) solution and a simple drying process on a hot plate (70 – 100 ℃) for a few minutes, and there is no need for a critical point drying (CPD) process.

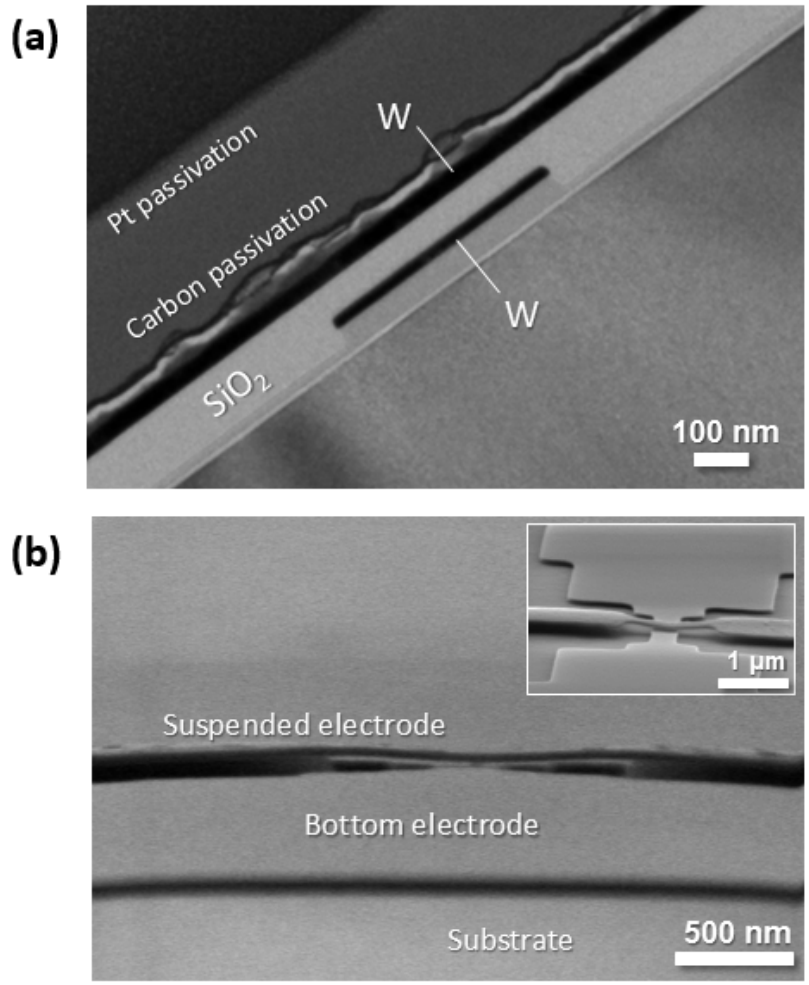

Fig S1. Fabrication results: (a) a cross-sectional TEM image of a fabricated device before the release process and (b) a SEM image (side view) of the fabricated device after the release process.

2. Resistivity Extraction

To determine the resistivity of the tungsten nanobeams, the total resistances of each device were evaluated by varying the length (L) and width (W) of the suspended beam. Figure S2 shows the linear extrapolation of the total resistance of each device. Here, the total resistance includes both the resistance of the nanobeam and the parasitic resistance that originates from the probing contacts and the lead lines that connect the nanobeam to the probing pads. Because the probing resistance is approximately a few ohms, the parasitic resistance is primarily determined by the tungsten lead lines. The y-axis intercept (120 Ω) corresponds to this parasitic resistance. Meanwhile, the slope of the fitted line is linearly proportional to the resistivity of the nanobeam and the dimensional parameters. Therefore, the resistivity of the nanobeam can be extracted from the coefficients of the fitted line. For the device groups with W = 300 nm and W = 180 nm, the resistivity ρ was calculated to be $2.56\times10^{-7}\ \Omega m$, which is larger than the bulk resistivity ($5.28\times10^{-8}\ \Omega m$). Finally, we found the conductivity of the tungsten nanobeam to be 5.39 $\times10^{6}$ Sm^{-1}.

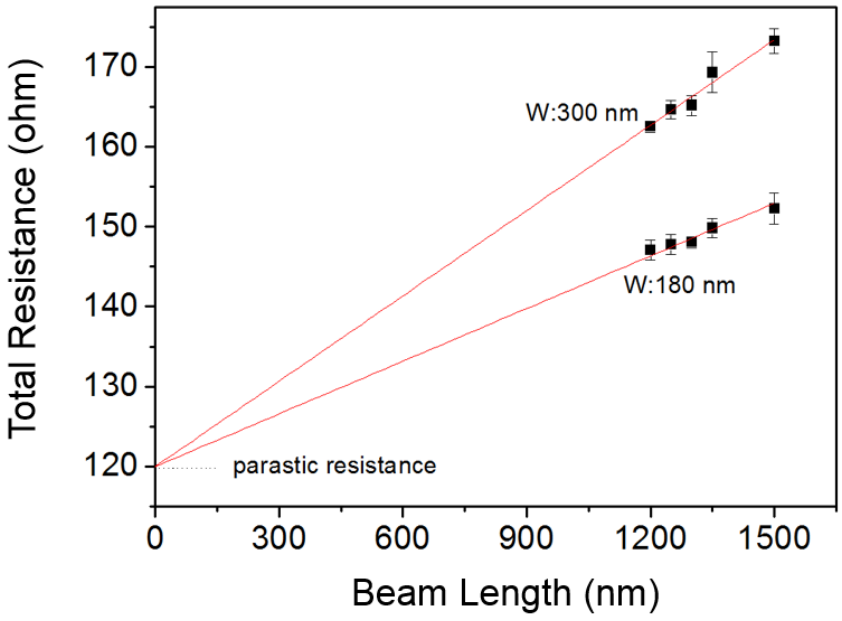

Fig S2. The total resistance of the device as a function of the device's dimensions. The solid red lines represent the linear extrapolations of the measurements (black squares). The error bars represent the standard deviations among the device ($n \geq 4$).

3. A One-dimensional (1-D) simplified Model

In the thermo-mechanical actuation process, resistive heating leads to a temperature increase, which in turn induces the mechanical operation of the nanostructure via thermal expansion. However, the measured result, which is represented by the current vs. the voltage curves (Figure 2 in the main manuscript), does not directly reveal the thermo-mechanical interactions and the effects of thermal concentration in detail. In fact, because of the large number of variables and material properties that contribute to our system, it is difficult to gain a complete understanding of the operation mechanism that underlies the thermo-mechanical interactions. To simplify this complicated situation, we considered the most intuitive 1-D model, which is shown in Figure S3. The advantage of this 1-D model is that the specific contribution of the concentrated electrothermal energy can be investigated in a simple manner with respect to the reduced thermal conductivity, which reflects the enhanced electron-phonon scattering effect.

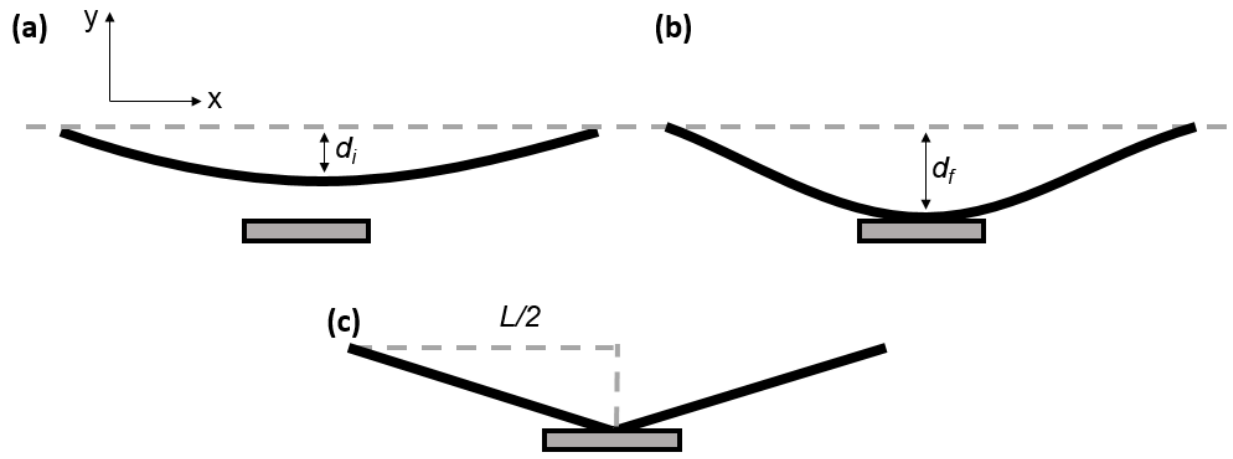

Fig S3. Schematic diagrams of the simplified one-dimensional model of the curved beam structure: (a) the initial state, (b) the final state and (c) a tapered shape approximation.

The initial state of the suspended nanobeam structure in which the initial downward deflection of d_i is induced by the residual stress is presented in Figure S3a. We define the final state of the device as shown in Figure S3b, and the corresponding deflection d_f is determined by the thickness of the sacrificial layer. For the case in which the total beam length satisfies $L >> d_i$, and $L >> d_f$, the extended profile of the beam can be simplified with a linear approximation, as shown in Figure S3c. In this linear approximation, the relation between the dimensional parameters satisfies

$$L_i \approx 2\times\sqrt{(\frac{L}{2})^2 + d_i^2} \qquad (1)$$

$$L_f \approx 2\times\sqrt{(\frac{L}{2})^2 + d_f^2} \qquad (2)$$

where L_i and L_f indicate the extended beam lengths in the initial state and the final state, respectively. Because the expansion of the beam length ΔL is induced by a temperature increase, it can be represented as

$$\Delta L = L_f - L_i = L_i \alpha \Delta T \qquad (3)$$

$$\Delta T_M = \frac{V^2/R}{12\kappa A/L} \qquad (4)$$

where α is the coefficient of the thermal expansion and ΔT_M is the temperature difference between the initial state and the final state. Equation (4) can be derived from the heat-transfer equation for the suspended beam structure. A is the cross-sectional area of the beam, and V and R are the applied voltage and the resistance of the device, respectively. In addition, α denotes the thermal conductivity of the nanowire. As described in the main manuscript, α can be calculated from the Wiedemann-Franz law using the resistivity determined in Section 2.

4. Three-dimensional (3-D) Finite-element-method (FEM) Simulation

In the main manuscript, we verified the agreement between the one-dimensional model analysis and the measured data. Note that (1) residual stress initiates the downward buckling and (2) the width of the beam is much greater than its thickness. Therefore, in our model analysis, the lateral displacement can reasonably be ignored. We assumed that the downward deflection dominates the displacement. The temperature and the downward displacement are particularly important parameters that govern the thermo-mechanical interactions. However, it is difficult to directly measure these parameters. Therefore, we independently investigated a three-dimensional (3-D) simulation and compared the results of the 1-D model with those of the 3-D model. We evaluated both models by varying the device dimensions. Figure S4 presents the validation of the 3-D FEM approach in comparison with the 1-D model. In the 3-D finite-element-method (FEM) model, we assumed that the temperature of the substrate remained constant at room temperature (297 K). The FEM structure considers the practical situation in which the device structures are thermally connected through the intermediate insulating layers. The nanobeam structure and the equivalent parasitic resistances are implemented as a combination of mesh structures. For the material properties of the tungsten nanowire, the value measured in Section 2 is employed, as in the 1-D model. The reduced thermal conductivity that is implied by the reduced electrical conductivity and the Wiedemann-Franz law is taken into account. Figure S4a and S4b depict the relations between the applied voltage and the absolute temperature and between the applied voltage and the downward displacement of the nanobeam structure. From these data, we verified that the two models (namely, the 1-D model and the 3-D model, which were developed independently) exhibit similar trends in their thermo-mechanical behavior. This finding enables us to trust the spatial energy distribution provided by the 3-D FEM analysis. Furthermore, this result addresses the uncertainty in the linear approximation that is assumed in the 1-D model.

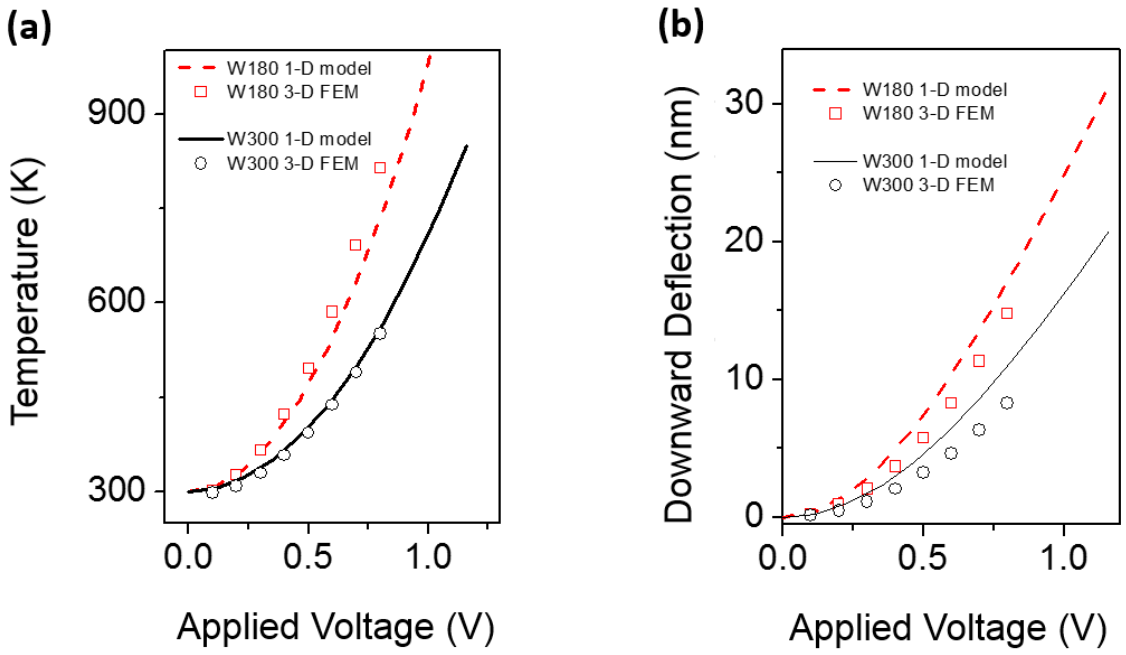

Fig S4. A Comparison of the 1-D and 3-D models for two device widths: (a) the temperature vs. the applied voltage and (b) the downward displacement vs. the applied voltage.

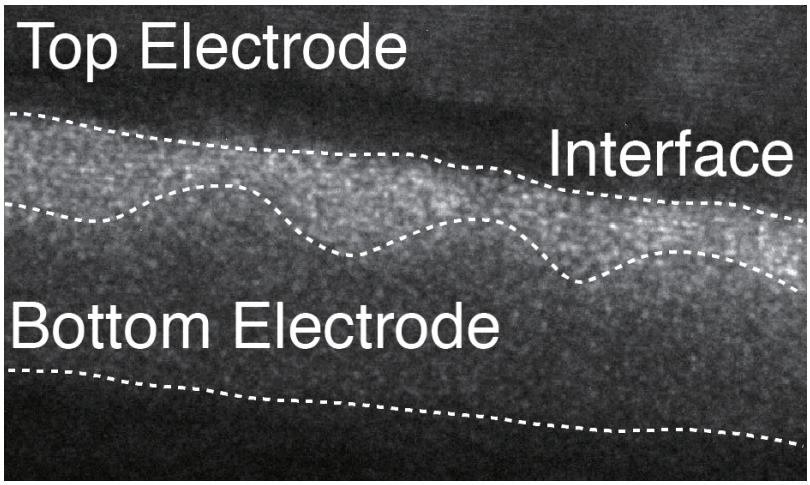

Fig. S5 A magnified TEM image of the contacting interface. At the critical contacting interface, the space between the top electrode and the bottom electrode is uniformly filled with low-density tungsten.

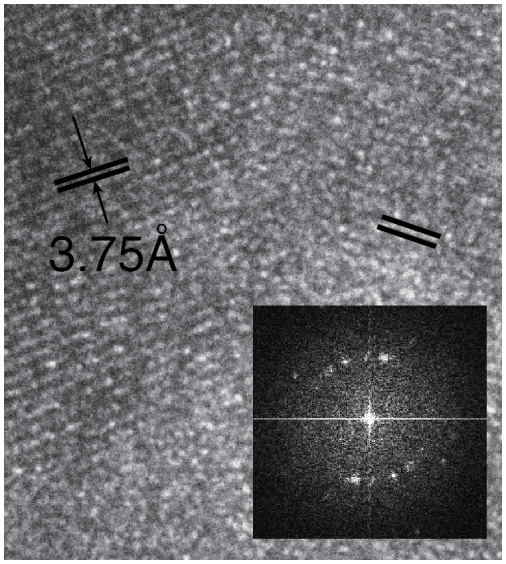

Fig. S6 A magnified TEM image of the native tungsten. The lattice of the tungsten structure is randomly oriented and FFT analysis (inset) shows irregular and indistinct pattern.

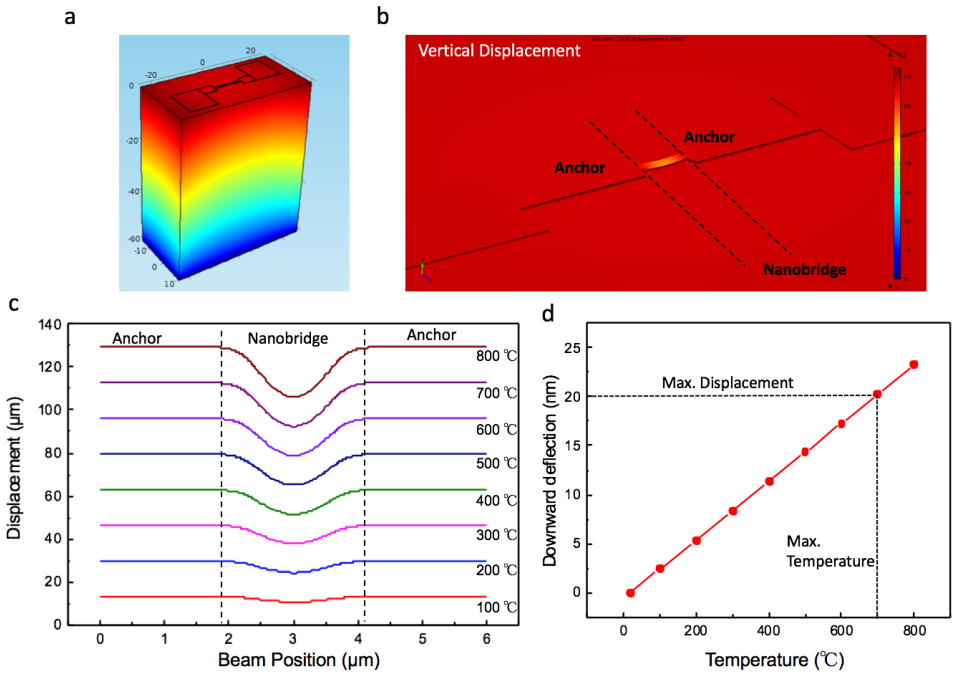

Fig S7. Thermal expansion analysis of ambient temperature effect. (a) A FEM simulation model. (b) 3-D mapping of the vertical displacement. (c) The beam profile along the ambient temperature increase. (d) Downward displacement vs. ambient temperature. The theoretical maximum temperature of operation is 700 °C.